

# Macroscopic Study on Current Transport Path in Front-Side Contacts of Crystalline Silicon Solar Cells

Shenghu Xiong, Xiao Yuan,\* Yunxia Yang, Jiefeng Zhang, Hua Tong, Cui Liu, Xiaojun Ye, Shengyong Li, Lan Luo, and Xianhao Wang

Double rectangular transmission line model and contact-end voltage measurement are used to study the variation in sheet resistance and current transfer length of the contact interface between the front-side electrode and the emitter of crystalline silicon solar cells during metallization. The current distribution and its relationship with the sheet resistances of the electrode, contact interface, and emitter are given at the macrolevel. The model shows that the current flows transversely for  $\approx 50\text{--}500\ \mu\text{m}$  in the highly conductive interface with a sheet resistance in the range of  $0.5\text{--}5\ \Omega\ \square^{-1}$  beneath the designed electrodes. The  $I\text{--}V$  curves beneath the front silver pad sintered at lower, optimum, and over-fired temperatures are always linear. However, they are nonlinear between the front-side and rear-side electrodes of the double phosphorus-doped N-type silicon substrates, which suggests that the contact type changes from Ohmic to Schottky. The experimental results imply that the photogenerated current on the emitter surface is mainly transferred transversely via the crystallites embedded in the shallow highly doped silicon layer rather than the deeper lightly doped contact area at the contact interface.

flows through the Ag–Si interface via these direct or indirect contact crystallites or colloids.<sup>[5–8]</sup> Few studies have used mathematical and physical models to analyze the conductive channels from the macroscopic perspective,<sup>[9]</sup> including the current distribution at the contact interface,  $I\text{--}V$  curve, current transfer length, and sheet resistance beneath the front electrode.

According to the traditional current transfer theory, in planar devices, current transport between a metal and a semiconductor is completed within a very short distance at the edge of the electrode.<sup>[10]</sup> The current transport path is clearly defined. A silicon solar cell is a large planar device. However, its contact interfaces differ considerably from that between metals and semiconductors. This is because, in the solar cell, the contact is mainly composed of sintered screen-printed silver paste. The phases and composition are complex

## 1. Introduction

Thus far, discussions on current transport between a silver electrode and silicon emitter have mostly been based on numerous scanning or transmission electron microscopy observations with detailed modeling and inference of the microscopic mechanism.<sup>[1,2]</sup> A large number of silver crystallites or colloids exist at the interfaces of samples with different morphologies,<sup>[3]</sup> sintering temperatures,<sup>[4]</sup> and doping concentrations.<sup>[1]</sup> A current

at the interface. The current transport path, transfer length ( $L_t$ ), and sheet resistance ( $R_{sk}$ ) beneath the electrode need to be clarified further.<sup>[11]</sup>

In this study, the double rectangular transmission line method, contact-end voltage measurements, and  $I\text{--}V$  tests were applied to characterize  $L_t$ ,  $R_{sk}$ , and current transport path including its distribution, through pertinent pattern and test fixtures. In addition, the rational and limitation of contact-end voltage measurement were discussed in detail to obtain reliable solutions from the model.

## 2. Experimental Section


The theoretical model is based on the double transmission line model and considers the influence of the internal resistance of the electrode and the sheet resistance below the electrode on current transmission.<sup>[12]</sup> As shown in **Figure 1**, the current flows from point 1 to the first electrode, from point 8 to the doped layer between the two electrodes, from point 7 to the second electrode, and from point 4 to the negative pole of the source meter. Four differential equations can be formulated to describe the distributions of current and voltage in the contact area by establishing a rectangular coordinate system with 0 as the origin.

$$\frac{dI_2(x)}{dx} = \frac{(V_1(x) - V_2(x))Z}{\rho_c} \quad (1)$$

Dr. S. Xiong, Prof. X. Yuan, Prof. Y. Yang, Dr. J. Zhang, Dr. H. Tong, Dr. C. Liu, Dr. X. Ye, Prof. S. Li  
School of Materials Science and Engineering  
East China University of Science and Technology  
Shanghai 200237, China  
E-mail: yuanxiao@ecust.edu.cn

Prof. L. Luo  
Shanghai Institute of Ceramics  
Chinese Academy of Science  
Shanghai 200131, China

Dr. X. Wang  
Research Microscopy Solutions Department  
Carle Zeiss (Shanghai) Co. Ltd.  
Shanghai 200131, China

 The ORCID identification number(s) for the author(s) of this article can be found under <https://doi.org/10.1002/pssa.201900480>.

DOI: 10.1002/pssa.201900480

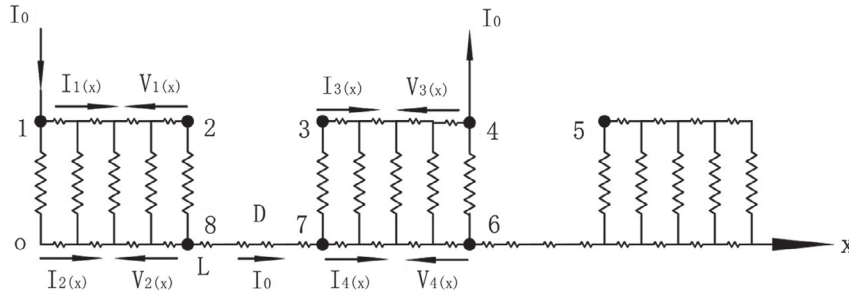


**Figure 1.** Double rectangular transmission line model schematic diagram.

$$\frac{dV_2(x)}{dx} = -I_2(x) \frac{R_{sk}}{Z} \quad (2)$$

$$\frac{dV_1(x)}{dx} = -I_1(x) \frac{R_{sm}}{Z} \quad (3)$$

$$\frac{dI_1(x)}{dx} + \frac{dI_2(x)}{dx} = 0 \quad (4)$$

where  $Z$  is the length of the electrode. The following differential equation can be obtained using the above simultaneous equations

$$\frac{d^2 I_2(x)}{dx^2} - \alpha^2 I_2(x) + \frac{R_{sm}}{\rho_c} I_0 = 0 \quad (5)$$

where

$$\alpha = \sqrt{(R_{sk} + R_{sm})/\rho_c} = 1/L_t \quad (6)$$

$R_{sk}$  is the sheet resistance under the electrode,  $R_{sm}$  is the square resistance of the electrode,  $\rho_c$  is the contact resistivity, and  $L_t$  is the transfer length. The solution of the second-order linear differential equation can be given as follows

$$I_2(x) = C_1 + C_2 e^{\alpha x} + C_3 e^{-\alpha x} \quad (7)$$

According to the boundary conditions

$$I_1(0) = I_0, I_2(0) = 0 \quad (8)$$

$$I_1(L) = 0, I_2(L) = I_0 \quad (9)$$

The values of the coefficients of  $C_1$ ,  $C_2$ , and  $C_3$  can be calculated, and then the current distributions  $I_1(x)$  and  $I_2(x)$  can be obtained. Using the current equations, the potential difference  $V_{37}$  between the electrode (point 3) and emitter (point 7) can be expressed as follows

$$V_{37} = V_3 - V_7 = \frac{\rho_c}{Z} \frac{dI_4(x)}{dx} \Big|_{x=P7} \quad (10)$$

which is theoretically identical to  $V_{28}$  (the potential difference between the points 2 and 8) in size and in the opposite direction. The model also introduced the contact-end resistance initially proposed by Shockley,<sup>[13]</sup> which is defined as  $R_{end} = \frac{V_{out}}{I_{input}} = \frac{V_{45}}{I_7}$ , where  $V_{45}$  is the potential difference between the electrode (point 4) and the emitter (point 5). Considering the fact that the value of

current is zero on the right side of point 6 and current flows through the first and second electrodes, potential of the third electrode (at point 5) can be considered to be equal to that at point 6.<sup>[14]</sup> Then,  $V_{45}$  can be considered to be approximately equal to the potential difference between points 4 and 6 ( $V_{46}$ ). Based on the definition, the following equation can be established

$$V_{45} = V_{43} + V_{37} = \frac{R_{sm}}{Z} \int_0^L I_1[x] dx + \frac{-\rho_c}{Z} \frac{dI_4(x)}{dx} \Big|_{x=P7} \quad (11)$$

where  $D$  is the distance between electrodes. The potential difference between the first electrode at point 2 and the second electrode at point 3 can be written as follows

$$V_{23} = \frac{\rho_c}{Z} \frac{dI_2(x)}{dx} \Big|_{x=P8} + I_0 R_{sh} \frac{D}{Z} - \frac{\rho_c}{Z} \frac{dI_4(x)}{dx} \Big|_{x=P7} \quad (12)$$

The potential difference between points 1 and 2 of the first electrode is

$$V_{12} = \frac{R_{sm}}{Z} \int_0^L I_1[x] dx \quad (13)$$

The values of  $V_{45}$ ,  $V_{23}$ , and  $V_{12}$  can be measured directly using the voltage probes. Equation (11)–(13) have four unknown parameters:  $R_{sm}$ ,  $R_{sk}$ ,  $\rho_c$ , and the sheet resistance of emitter  $R_{sh}$ .  $R_{sm}$  can be directly measured using a four-probe square resistance tester and  $R_{sh}$  is semiquantified (the range of the values are known when the samples are removed from the diffusion furnace in the factory and measured by the four-probe method). Thus, there are three unknowns to be determined. Assuming that the value of  $R_{sk}$  between the adjacent electrodes is equal,  $R_{sh}$  and  $\rho_c$  are uniform around the two adjacent electrodes.  $R_{sk}$ ,  $R_{sh}$ , and  $\rho_c$  can be obtained using Equation (10)–(12).  $L_t$  can be obtained using Equation (6). As shown in **Figure 2**,

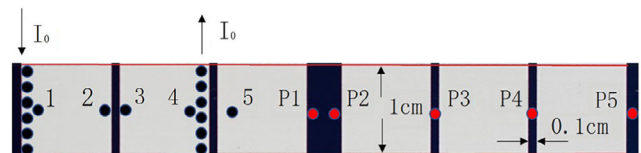


**Figure 2.** Schematic of sample and probe positions. Points 1–5 are potential probes, and points P1–P5 are probe positions for contact-end voltage measurement.

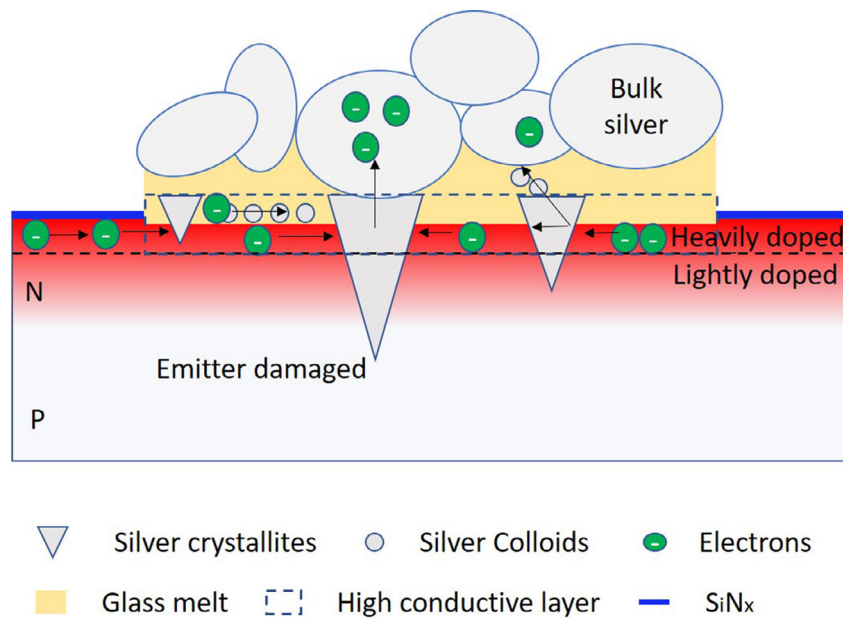


**Figure 3.** Schematic of the current transport path. Electrons flow from the side of the crystallites to the electrode by direct contact or quasidirect contact in the highly doped layer. Few electrons entered the silver crystallites from the lightly doped region and were then transferred to the electrode.

the probe positions corresponding to  $V_{12}$ ,  $V_{23}$ ,  $V_{34}$ , and  $V_{45}$  are marked.

**Figure 3** shows a schematic of the phase distribution at the contact interface and the possible transport path of photogenerated electrons under illumination. The aforementioned model is used to solve the electrical parameters of the interface.

The test pattern was carefully designed. To increase the proportion of contact voltage in the measurement and deduce the current transport path and current distribution, the length of the silver electrodes was extended, and the gap between the electrodes was reduced. To ensure that the current is uniformly transmitted in the electrode in a transverse direction, parallel probes were used for the input and output current. The positions of the probes are shown in **Figure 2**. The current and voltage were measured directly using a digital source meter Keithley 2602B. The probes were gold plated.

The experimental substrates were P-type( $N^+$  emitter) monocrystal silicon solar cells, and these were divided into two groups. The substrates in one group were covered by a passivation layer of  $\text{SiN}_x$  and those in the other group had no passivation layer; however, they had a naturally formed thin  $\text{SiO}_x$  film. The sheet resistance was  $90\text{--}100\ \Omega\ \square^{-1}$ , and the surface concentration was  $1\text{--}2 \times 10^{20}\ \text{cm}^{-3}$ . Commercialized burnt-through silver paste and evaporated silver were used for metallization. The samples screen printed with silver paste were metallized in a box-type infrared rapid annealing furnace at six temperatures, 600, 660, 690, 720, 750, and 780 °C. After sintering or evaporation, the samples were cut into squares with a width of 1 cm for measurement, as shown in **Figure 2**.

In addition, to determine the variation of the  $I$ – $V$  curves during the sintering process, N-type double-sided phosphorus-doped diffused samples were prepared, which had the same surface doping concentration as the  $N^+$  emitter cells.

### 3. Results and Discussion

#### 3.1. Selection of Test Current

The photogenerated current density of a monocrystalline silicon solar cell is  $\approx 40\ \text{mA cm}^{-2}$ . If the photogenerated current is simulated completely, the output current of the source meter is  $\approx 4\ \text{mA}$ , which is difficult for the reliable measurement of voltage. Thus, the current–voltage relationship between two adjacent electrodes was initially measured to determine whether there is a nonlinear  $I$ – $V$  relationship.<sup>[15]</sup> **Figure 4** shows the

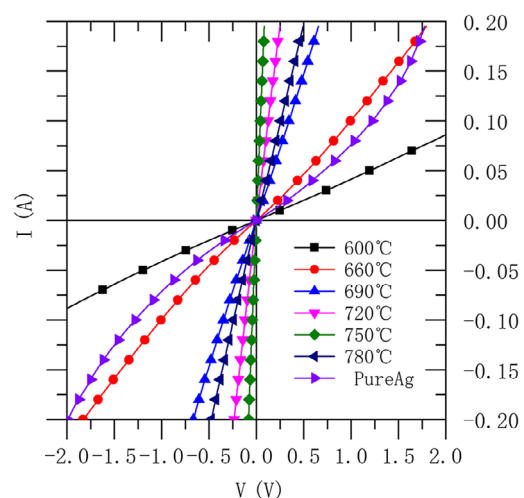


**Figure 4.**  $I$ – $V$  curves of the adjacent two electrodes on  $\text{SiN}_x$ -deposited emitter surface. The curves of sintered samples below 690 °C show a weak nonlinear effect, whereas the evaporated sample shows a significant nonlinear relationship.

curves in the absence of emitter resistance, which accounted for a majority of the measured voltage. Then, the influence of contact voltage would be amplified. The emitter resistance was calculated by setting  $R_{sh} = 95 \Omega \square^{-1}$ . The current range was  $\pm 0.2$  A. It was clear that the  $I$ - $V$  curves of the sintered electrodes below  $690^\circ\text{C}$  exhibited a weak nonlinear effect, and the slope variation was small. Thus, these curves could be treated as approximately linear. The curves of evaporated pure silver electrodes showed a significant nonlinear relationship. For comprehensive consideration, the measurement current of  $I_0$  was set to  $0.1$  A, which did not hinder judgment.

### 3.2. Measurement Results

Table 1 and 2 list the average measured values of  $V_{12}$ ,  $V_{23}$ ,  $V_{34}$ ,  $V_{45}$ , and  $R_{sm}$  when the emitter surface was covered with  $\text{SiN}_x$  and when it was not covered. Each average was obtained from 20 measurements using the pulse current method. It is clear that while  $R_{sm}$  decreased gradually with an increase in the temperature,  $V_{23}$  and  $V_{45}$  had significant inflection points at  $\approx 750^\circ\text{C}$ . The results indicated that the contact resistance between the electrode and the emitter surface decreased initially and then increased during sintering, which is consistent with the trend of  $I$ - $V$  curves at different metallization temperatures shown in Figure 4.

In the early sintering stage, especially below  $660^\circ\text{C}$ , the  $\text{SiN}_x$  layer present between the silver electrode and the emitter hindered the movement of electrons.<sup>[11]</sup> The differences and trends of measurement values between Table 1 and 2, especially with respect to the contact-end voltage  $V_{45}$ , reflect the effect of  $\text{SiN}_x$  layer and indicate that it was difficult to form contact, even without the  $\text{SiN}_x$  layer.

Because the measurements of the contact-end voltage affected the final solutions,<sup>[14,16]</sup> we used a probe to directly measure the potential difference between point 4 and the emitter surface in the absence of the  $\text{SiN}_x$  layer. In addition, we changed the distance between them to further confirm the reliability and accuracy of  $V_{45}$ . The positions, marked as P1–P5, are shown in Figure 2. The measurement results are shown in Figure 5. It was found that the increasing trend of  $V_{45}$  was nonlinear (absolute value) with the increase in distance. Especially, in samples with better contact,  $V_{45}$  increased up to 2.5 times. The inflection point was located at P2.

Theoretically, the measured values of  $V_{45}$  should not be related to the location of the probe P1–P5. The nonlinear increase indicated that there was current inflow on the right side of the second electrode at point 6 (in Figure 1), and the current density on the right side was inversely proportional to the

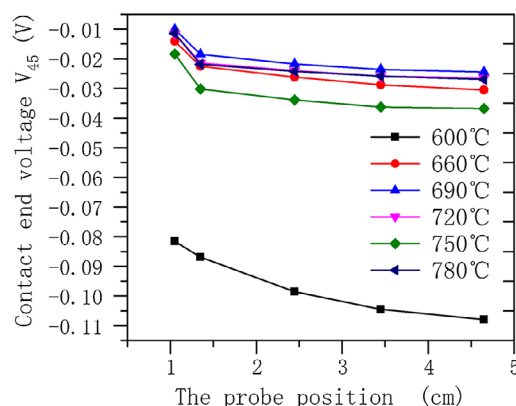


Figure 5. Relation of contact-end voltage  $V_{45}$  and probe-placed positions.

Table 1. Average measurements of  $V_{12}$ ,  $V_{23}$ ,  $V_{34}$ ,  $V_{45}$ , and  $R_{sm}$  of the samples with  $\text{SiN}_x$ .

Temperatures [ $^\circ\text{C}$ ]	600	660	690	720	750	780
$V_{12}$ [mV]	0.1731	0.162	0.16	0.137	0.14	0.138
$V_{23}$ [V]	4.463244	2.129933	1.473477	1.176003	1.067686	1.140029
$V_{34}$ [mV]	0.176	0.168	0.162	0.131	0.144	0.142
$V_{45}$ [V]	-0.100442	-0.018548	-0.005852	-0.004481	-0.003664	-0.006242
$R_{sm1}$ [m $\Omega$ ]	2.198	2.002	1.948	1.787	1.697	1.703
$R_{sm2}$ [m $\Omega$ ]	2.243	2.015	1.946	1.774	1.744	1.712

Table 2. Average measurements of  $V_{12}$ ,  $V_{23}$ ,  $V_{34}$ ,  $V_{45}$ , and  $R_{sh}$  of the samples without  $\text{SiN}_x$ .

Temperatures [ $^\circ\text{C}$ ]	600	660	690	720	750	780
$V_{12}$ [mV]	0.163	0.162	0.153	0.148	0.146	0.141
$V_{23}$ [V]	3.083398	1.605412	1.275565	1.140534	1.308872	1.199277
$V_{34}$ [mV]	0.168	0.164	0.155	0.153	0.151	0.146
$V_{45}$ [V]	-0.049018	-0.011344	-0.006445	-0.008793	-0.009787	-0.008706
$R_{sm1}$ [m $\Omega$ ]	1.929	1.844	1.784	1.803	1.793	1.728
$R_{sm2}$ [m $\Omega$ ]	1.971	1.919	1.808	1.858	1.844	1.775

distance. With better contact and the potential ratio induced by the current flowing on the right, the measured values of  $V_{45}$  increased gradually. For the potential difference between 1.05 and 1.35 cm, the estimated current was  $\approx 0.3$  mA, accounting for 3% of the test current. The significance of these measurements will be discussed later. When the probe was fixed, the value of  $V_{45}$  at different temperatures followed the same trend as in Table 1 and 2, which varied with the metallization temperature and had sufficient selectivity. The systematic error of contact-end voltage measurement did not affect its discrimination for different samples.

### 3.3. Numerical Solutions of $R_{sh}$ , $L_t$ , $R_{sk}$ , and $\rho_c$

The values of  $R_{sh}$  of the samples varied between 90 and  $100 \Omega \square^{-1}$ , which can be used as a benchmark to determine the accuracy of the theoretical model compared with the extracted  $R_{sh}$ . Figure 6 shows that the numerical solution of  $R_{sh}$  deviated far from the known scope of  $R_{sh}$ , especially for samples sintered at low temperatures below  $720^\circ\text{C}$ . After subtracting the emitter resistance between points 2 and 3, the measured value of  $V_{23}$  was much larger than the voltage obtained using Equation (10). The value of  $V_{45}$  did not fully represent the potential loss between points 7 and 4 (or points 1 and 7), the voltage loss was reflected in the numerical solution of  $R_{sh}$ . According to the interface analysis of sintering,  $\text{SiN}_x$  existed mostly at temperatures lower than  $660^\circ\text{C}$ . It can be approximated that the value of  $R_{sk}$  is still equal to  $R_{sh}$ . Therefore, the model can be approximately modified to [17]

$$V_{23} = I_0 \frac{R_{sh}}{Z} (d + 2L_t) \quad (14)$$

Thus, assuming that both  $R_{sh}$  and  $R_{sk}$  are  $95 \Omega \square^{-1}$ , we can calculate the value of  $L_t$  at  $600^\circ\text{C}$ , which is  $0.112$  cm, and that of  $\rho_c$  is  $1.19 \Omega \text{cm}^2$ , which are consistent with the existence of  $\text{SiN}_x$ . The current flowed at a length of approximately  $L_t$  beneath the electrode.

Around the optimal sintering temperature, the  $\text{SiN}_x$  and  $\text{SiO}_x$  layers were etched away and sufficient conductive channels were established. The solution of  $R_{sh}$  was close to the values provided by the cell manufacturer, and the contact resistivity was between  $2 \times 10^{-4}$  and  $5 \times 10^{-3} \Omega \text{cm}^2$ . The corresponding value of  $L_t$  varied between 50 and  $500 \mu\text{m}$  and that of  $R_{sk}$  was

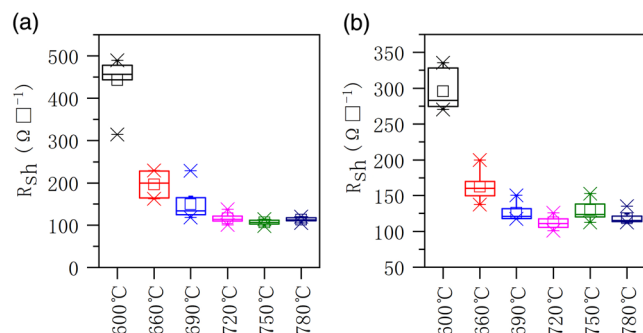


**Figure 6.** Numerical solutions of  $R_{sh}$ . a)  $\text{SiN}_x$ -covered emitter. b) Emitter without  $\text{SiN}_x$  (covered by one thin  $\text{SiO}_x$  layer formed in air).

basically distributed in the range of  $0.5\text{--}5 \Omega \square^{-1}$ . It is shown that the width of  $L_t$  is considerably greater than the current electrode fingers width ( $\approx 45 \mu\text{m}$ ), which is why the traditional transmission line method can obtain reasonable results when calculating the contact resistivity (this method directly multiplies the measured contact resistance with the contact area per unit to obtain the contact resistivity<sup>[18]</sup>). Despite some deviations, the model reflected the objective changes in metallization and was reliable.

In the aforementioned discussion, the measurements of  $V_{45}$  were related to the distance of two probes caused by the current flowing on the right side. Figure 7a,b shows the effect of  $V_{45}$  on  $\rho_c$ ,  $R_{sk}$ ,  $R_{sh}$ , and  $L_t$  considering that optimal fired samples were not covered with  $\text{SiN}_x$  at  $720^\circ\text{C}$  as an example (judged from the numerical extraction of  $R_{sh}$ ). The right-side data shown using circles were calculated using the hypothetical value of  $V_{45} = 0.005$  V. The value of  $\rho_c$  was sensitive to the variation in  $V_{45}$ , whereas  $R_{sh}$ ,  $R_{sk}$ , and  $L_t$  were relatively insensitive. An appropriate fixed distance test helped in obtaining stable and differentiate contact resistivity, whereas the accuracy of the model still requires improvements.

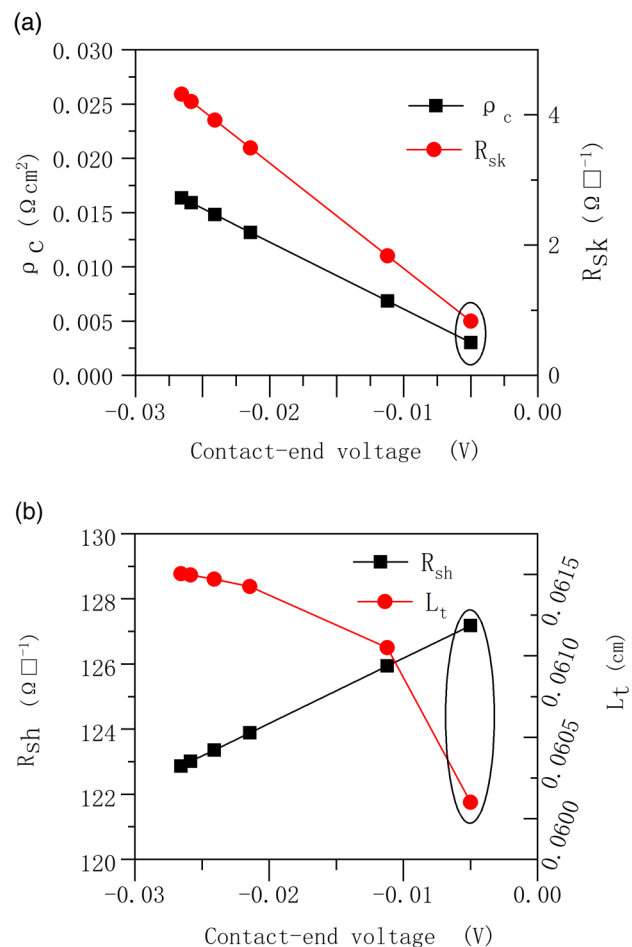


**Figure 7.** The effect of  $V_{45}$  measurements on  $\rho_c$  and  $R_{sk}$ . a)  $\rho_c$  and  $R_{sk}$ ; b)  $R_{sh}$  and  $L_t$ .



### 3.4. Current Distribution of Contact Interface

The current distribution in the electrode and the contact interfaces at different sintering temperatures can be determined from the average values of the above parameters. In **Figure 8**, the representative sintering temperatures of 600, 750, and 780 °C are taken as examples. Below 750 °C, the transfer length decreased gradually with an increase in temperature; however, it increased again above 750 °C. The shorter the transfer length, the lower the cell power loss.

The photogenerated current on the surface of the actual cells flows from both sides of the finger grid. The current distribution is also regulated by  $R_{sm}$ ,  $R_{sk}$ , and  $\rho_c$ .

### 3.5. Current Transport Path of Contact Interface

Figure 8 shows that the numerical solution of the theoretical model indicated that the current flowing from the electrode at point 1 passed through the electrode and the interface layer below the electrode, before it entered the emitter surface. The transmission distance could be approximately considered as the transfer length  $L_t$ . **Figure 9a,b** shows their distributions obtained using numerical solutions. The model indicates that the current traveled the length of  $L_t$  in a highly conductive layer

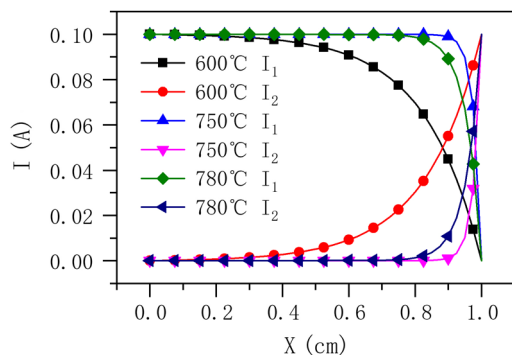


**Figure 8.** Current distributions in the electrode and highly conductive layer of the samples sintered at 600, 750, and 780 °C. Transfer length decreases gradually for firing temperatures between 600 and 750 °C but increases for firing temperatures above 750 °C.

with square resistance nearly 20 times smaller than  $R_{sh}$  under the electrode, as shown in **Figure 9c,d**.

The scanning electron microscopy photographs of the contact interfaces of samples with no  $\text{SiN}_x$  layer showed that the number of silver crystallites at the top or the edges of the pyramid increased gradually, as shown in **Figure 10**. It also corresponded to the decrease in contact resistivity below the over-firing temperature and was in accordance with the  $\text{SiN}_x$ -covered samples.<sup>[11]</sup> The current was mostly transmitted to the silver electrode through direct or quasidirect contact of the crystallites,<sup>[6]</sup> which forms the physical basis of the larger  $L_t$ .

The high conductivity layer under the electrode is a complex system formed by silver crystallites (including colloids), glass melt, and a heavy doping layer. The current was mainly conducted from the left or right of the crystallites to the electrodes. We designed an experiment to determine the principal path of electron transmission. Double-sided phosphorus-doped N-type silicon substrates were fabricated with the same front structure as P-type cells. Phosphorus was also doped on the rear side of the samples to facilitate Ohmic contact. The samples were printed with the same commercial paste and sintered at the same temperature. Then, the rear side of the sintered samples was scrubbed with HF 5% solution and then coated with GaSn liquid metal after drying. The  $I$ - $V$  curves of the samples were measured between the front and rear electrodes. Under this condition, the current transferred from the bottom of the contact crystallites to silicon. It was found that the  $I$ - $V$  curves changed from linear to nonlinear above 720 °C, as shown in **Figure 11a**, where a typical Schottky contact was formed. The reverse breakdown voltage was greater than 20 V, and the reverse saturation current increased significantly with an increase in the sintering temperature. A significant forward breakdown voltage of  $\approx 5$  V was observed. Whether the applied bias was positive or negative, the electrons transport was hindered in over-fired samples.

**Figure 12** shows the cross-sectional images of the contact interface sintered at 600, 720, and 780 °C, respectively. At 600 °C, most of the passivation layer of  $\text{SiN}_x$  with a thickness of  $\approx 70$  nm existed at the interface; however, the glass melt in some areas started penetrating it. At 720 °C, little amounts of  $\text{SiN}_x$  remained, where direct or quasidirect contact formed at many locations. At 780 °C, only few locations had direct or

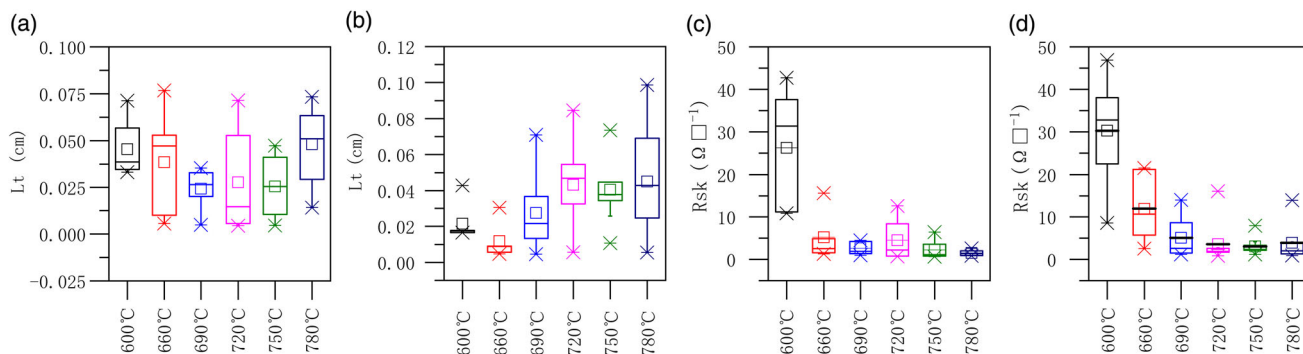


**Figure 9.** Relationship among  $L_t$ ,  $R_{sk}$ , and sintered temperatures of two types of samples. a)  $L_t$  with  $\text{SiN}_x$ . b)  $L_t$  without  $\text{SiN}_x$ . c)  $R_{sk}$  with  $\text{SiN}_x$ . d)  $R_{sk}$  without  $\text{SiN}_x$ .

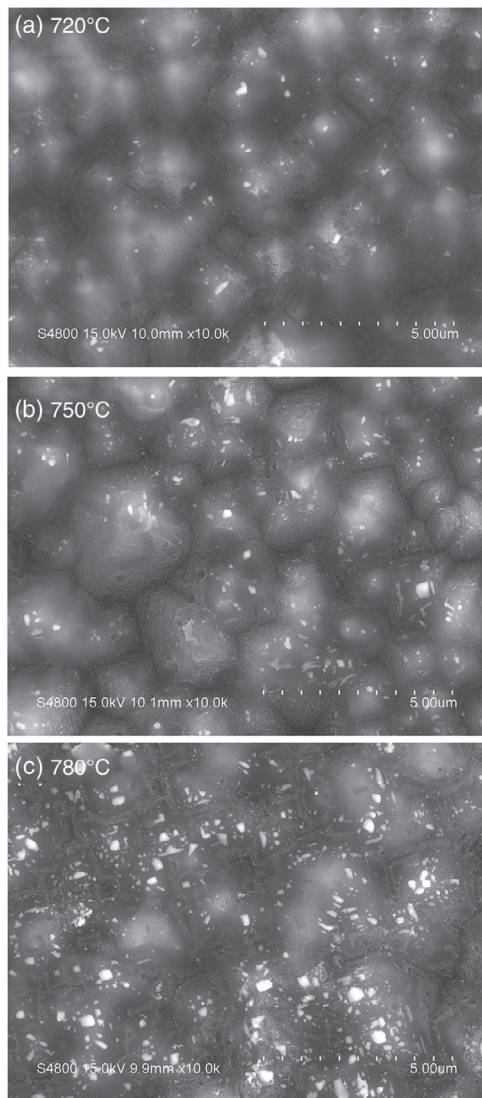


**Figure 10.** Distribution of silver crystallites (small white areas) on the top of the pyramids at the contact interface of the samples without  $\text{SiN}_x$ . a) Few crystallites at 720 °C. b) Few more crystallites at 750 °C. c) Excessive amount of crystallites at 780 °C.

quasidirect contact, and the thickness of the glass layer was mostly above 100 nm. It can be inferred that the nonlinear  $I$ - $V$  curves originated because of the low doping concentration (when the highly doped layer was etched away) and the thick glass melt (doped with silver crystallites or colloids).

The current would mainly be transferred from the side of the contact spots in the highly doped area to the electrode for the optimally fired samples at  $\approx 750$  °C, and it was rarely transferred via the lightly doped contact area, as shown in Figure 3. The thickness of the highly doped layer was  $\approx 50$  nm. This was problematic as more silver crystallites must be formed on the emitter surface for the transverse current transfer, whereas the penetration depth of silver crystallites should be controlled to reduce junction leakage or shunting. The entire emitter surface covered with small silver particles or tiny colloids was the only

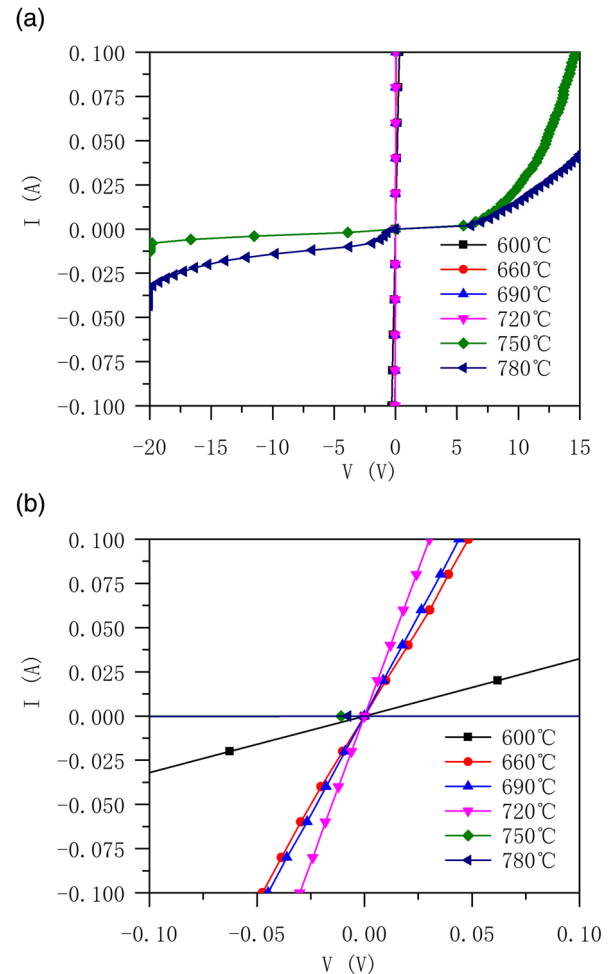


**Figure 11.**  $I$ - $V$  curves measured between front and rear electrode of double-side phosphorus-doped N-type silicon. a) Complete curves. b) Magnification around the origin of the coordinate.

ideal contact. Surface morphology and defects,<sup>[19,20]</sup> including those arising from process conditions, would result in silver particles of different sizes, which will damage the emitter to various extents and block the transport of electrons.

## 4. Conclusions

The double transmission line model along with contact-end voltage measurement was used to objectively characterize the current transport path of front contact interfaces in silicon solar cells during metallization. It was shown that the current transversely flowed to  $\approx 50 \mu\text{m} \leq L_t \leq 500 \mu\text{m}$  in a complex relatively highly conductive interface, comprising a heavily doped layer, silver crystallites (including silver colloidal particles), and glass melt with a sheet resistance of  $\approx 0.5 \Omega \square^{-1} \leq R_{sk} \leq 5 \Omega \square^{-1}$  beneath the electrodes in the designed pattern. The comparisons of  $I$ - $V$  curves between the silver electrodes on the emitter surface and the front and rear electrodes in the double-sided phosphorus-doped N-type silicon substrates indicated that the electrons

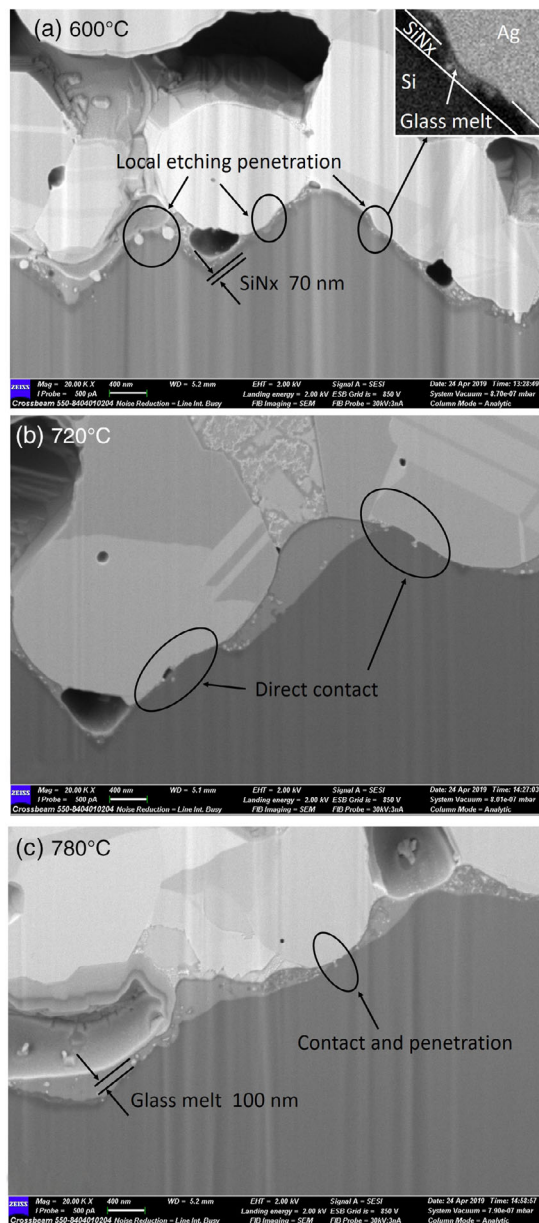


**Figure 12.** Cross-sectional focused ion beam-scanning electron microscopy (FIB-SEM) images of Ag-Si contacts sintered at different temperatures. a) 600, b) 720, and c) 780 °C.

were mainly transferred from the shallow, highly doped area to the embedded crystallites and then to the electrode. A Schottky contact was formed between the silver crystallites and the deeper, lightly doped area, blocking the electron transport from the bottom. The model and experimental results show that the performance of silver paste can be further improved by reducing the paste corrosion to the emitter, increasing the precipitation of silver particles with shallow penetration depth, and reducing the sheet resistance of the electrode. In addition, the reliability and selectivity of the contact-end voltage measurements were

sufficient to distinguish between the samples contacted in various degrees, although the accuracy must be enhanced further.

## Acknowledgements

This study was supported by the National High Technology Research and Development Program of China (grant no. 2014AA052101).

## Conflict of Interest

The authors declare no conflict of interest.

## Keywords

contact-end voltages, contact resistivities, current transport paths, solar cell metallization, transfer lengths

Received: June 19, 2019

Revised: September 17, 2019

Published online:

- [1] G. Schubert, *Ph.D. Thesis, University at Konstanz, Konstanz* **2006**, pp. 66–77.
- [2] R. Hoenig, *Ph.D. Thesis, Fraunhofer Institute for Solar Energy Systems ISE, Freiburg*, **2014**, pp. 159–173.
- [3] P. Kumar, B. Willsch, M. Drschabel, Z. Aabdin, R. Hoenig, N. Peranio, F. Clement, D. Biro, O. Eibl, *Energy Procedia*, **2015**, 67, 31.
- [4] J. Qin, W. Zhang, S. Bai, Z. Liu, *Appl. Surf. Sci.* **2016**, 376, 52.
- [5] C. Ballif, D. M. Hujic, G. Willeke, A. Hessler-Wyser, *Appl. Phys. Lett.* **2003**, 82, 1878.
- [6] E. Cabrera, S. Olibet, J. Glatz-Reichenbach, R. Kopecek, D. Reinke, G. Schubert, *J. Appl. Phys.* **2011**, 110, 114511.
- [7] Z. G. Li, L. Liang, A. S. Ionkin, B. M. Fish, M. E. Lewittes, L. K. Cheng, K. R. Mikeska, *J. Appl. Phys.* **2011**, 110, 074304.
- [8] M. Pfeffer, P. Kumar, O. Eibl, *J. Electron. Mater.* **2016**, 45, 5764.
- [9] D. K. Schroder, D. L. Meier, *IEEE Trans. Electron Devices* **1984**, 31, 637.
- [10] H. Berger, *Solid-State Electron.* **1972**, 15, 145.
- [11] S. Xiong, X. Yuan, H. Tong, Y. Yang, C. Liu, X. Ye, Y. Li, X. Wang, L. Luo, *Solid-State Electron.* **2018**, 142, 1.
- [12] J. D. Kim, K. S. Nam, J. G. Koo, *Int. J. Electron.* **1996**, 81, 285.
- [13] W. Shockley, *Research and Investigation of Inverse Epitaxial UHF Power Transistors*. Number Report No. AI-TOR-64-207. Air Force Atomic Laboratory, Wright-Patterson Air Force Base, OH **1964**, 113–140.
- [14] D. Alok, B. J. Baliga, P. K. McLarty, in *Proc. IEEE Int. Electron Devices Meeting*, IEEE, Washington, DC **1993**, pp. 691–694.
- [15] D. K. Schroder, *Semiconductor Material and Device Characterization*, 2nd ed., John Wiley & Sons Dalian, China **2008**, Ch. 3.
- [16] C. Xu, J. Wang, M. Wang, H. Jin, Y. Hao, C. P. Wen, *Solid State Electron.* **2006**, 50, 843.
- [17] G. S. Marlow, M. B. Das, *Solid State Electron.* **1982**, 25, 91.
- [18] P. N. Vinod, *J. Mater. Sci. Mater. Electron.* **2011**, 22, 1248.
- [19] A. Khanna, P. K. Basu, A. Filipovic, V. Shanmugam, C. Schmiga, A. G. Aberle, T. Mueller, *Sol. Energy Mater. Sol. Cells* **2015**, 132, 589.
- [20] E. Cabrera, S. Olibet, D. Rudolph, P. E. Vullum, R. Kopecek, D. Reinke, C. Herzog, D. Schwaderer, G. Schubert, *Prog. Photovoltaics* **2015**, 23, 367.